PHOTONICS Research

Photonics-enabled distributed MIMO radar for high-resolution 3D imaging

Jingwen Dong,[1] Qiang Sun,[1,2] Zekun Jiao,[1] Liqi Zhang,[1,2] Ziqiang Yin,[1,2] Jiajie Huang,[1,2] Jinghan Yu,[3] Shu Wang,[3] Shangyuan Li,[3] Xiaoping Zheng,[3] and Wangzhe Li[1,2,*]

[1]National Key Laboratory of Microwave Imaging Technology, Aerospace Information Research Institute, Chinese Academy of Sciences, Beijing 100190, China
[2]School of Electronics, Electrical and Communication Engineering, University of Chinese Academy of Sciences, Beijing 100049, China
[3]Beijing National Research Center for Information Science and Technology, Department of Electronic Engineering, Tsinghua University, Beijing 100084, China
*Corresponding author: wzli@mail.ie.ac.cn

Received 30 March 2022; revised 18 May 2022; accepted 28 May 2022; posted 31 May 2022 (Doc. ID 459762); published 30 June 2022

Three-dimensional (3D) imaging radar is an advanced sensor applied in space surveillance and target recognition for supplying 3D geometric features and supporting visualization. However, high 3D resolution requires both broadband operation and a large 2D aperture, which are difficult and complex for conventional radars. This paper presents a photonics-enabled distributed multiple-input and multiple-output (MIMO) radar with a centralized architecture. By use of photonic multi-dimensional multiplexing, multi-channel signal generation and reception are implemented on a shared reference signal in a central office, enabling a highly coherent network with a simple structure. Additionally, a sparse array and a synthetic aperture are combined to efficiently reduce the required transceivers, further weakening the dilemma between system complexity and angular resolution. A 4 × 4 MIMO radar is established and evaluated in field tests. A high-resolution 3D image of a non-cooperative aircraft is obtained, in which rich details are displayed. From a comparison with electronics-based radar, significant resolution improvement is observed. The results verify the superior imaging capability and practicability of the proposed radar and its great potential to outperform conventional technologies in target classification and recognition applications. © 2022 Chinese Laser Press

https://doi.org/10.1364/PRJ.459762

1. INTRODUCTION

Three-dimensional (3D) imaging radar is considered as an essential sensor for all-time and all-weather space surveillance, surveying and mapping, target classification and identification, etc. Compared with traditional two-dimensional (2D) imaging radar, such as inverse synthetic aperture radar (ISAR), it can provide more geometric features and better visualization through 3D energy distribution of scatterers [1–6]. To achieve high resolution in three dimensions, both a broad operating band and a large aperture are required, corresponding to range and angular resolutions, respectively, and the latter is commonly realized by a sparsely distributed antenna array. However, with an ever-increasing demand on 3D resolution, conventional radar arrays based on pure electronics have been encountering significant challenges: (1) the bandwidth of radar signal generation, distribution, reception, and processing is severely limited; (2) coaxial transmission loss becomes unbearable as array coverage enlarges; (3) coherence among widely separated array nodes is hardly guaranteed under the synchronization errors relying on the Global Navigation Satellite System (GNSS) or other wireless methods; (4) system cost and complexity inevitably increase with more array nodes needed due to aperture size requirement and sparsity constraint [7,8]. To resolve these issues, fast growing technologies based on the cross-fertilization between microwave photonics and radar arrays provide promising solutions [9–17]. The intrinsic ultra-wide bandwidth of photonics has been deeply applied in radar imaging and extensively validated to improve range resolution. Moreover, by virtue of multi-dimensional multiplexing, low-loss and high-capacity transmission, and phase-stable distribution, microwave photonics would enable centralized architecture via highly coherent fusion of multi-node signals as well as a large-scale array with much simpler implementations. These specialties permit a larger equivalent aperture and wider observation angle, leading to improved angular resolution and superior spatial diversity.

Recently, researches on photonics-enabled radar array have been intensively conducted [18–25]. In Ref. [19], a collocated multiple-input and multiple-output (MIMO) radar is demonstrated. Based on orthogonal frequency-division multiplexing

(OFDM) transmitting and wavelength-division multiplexing receiving, a linear equivalent aperture is formed by just a few transceivers to achieve high azimuth resolution. In Ref. [21], another MIMO radar is established in a real port for 2D maritime surveillance. Benefitting from the high signal stability among a deployed distributed fiber-optic network, both spatial resolution and monitoring capabilities are evaluated to be enhanced. In Ref. [23], a further expanded radar array up to 12 km is reported, which employs a fiber-based time–frequency synchronization network for full coherent detection. High resolution and high signal-to-noise ratio (SNR) are simultaneously realized in 2D imaging in the laboratory. Additionally, 3D imaging in near and far fields is experimentally demonstrated, in which a photonics-enabled 2D aperture is constructed to obtain scattering characteristics in azimuth and elevation directions [24,25]. All these researches show the great potential of photonics to bring unprecedented imaging performance, due to its possibilities of centralized processing and coherent fusion of multi-channel signals. On the other hand, in effectuating these possibilities, multiple reference signal matching with different channels should be independently generated in a central office (CO) and transferred to corresponding receivers (RXs) for separate processing, whether de-chirping or downconverting. Even in some distributed systems, accessional synchronizing signals, such as time and frequency signals or gate signals, are inescapably delivered to remote stations. Considering that more channels are needed for a larger aperture and high angular resolution under unambiguous and sparsity requirements, the above operations undoubtedly intensify the contradiction between system complexity and resolution.

To overcome such a dilemma, a photonics-enabled distributed MIMO radar for high-resolution 3D imaging is proposed based on the following two steps. First, a novel centralized architecture is designed based on the conjunctive multiplexing of time, frequency, and wavelength divisions. Both generation of multi-channel orthogonal signals and de-chirping reception of reflected echoes are implemented on a common reference signal in the CO. Thus, the photonic signals are transmitted over fibers, and the only task for transceivers is the signal conversion between photonics and electronics. In this way, structures of the remote station and the CO are simplified while maintaining high inter-channel coherence and low transmission loss for a long baseline. Second, with the efficient combination of compressed sensing (CS)-based super-resolution algorithms and traditional ISAR imaging methods, a sparse array and a synthetic aperture are jointly utilized to reduce the number of required transceivers, which further alleviates the aforementioned contradiction. X-band 4×4 distributed radar is established and evaluated in field tests. 3D imaging of real non-cooperative aircrafts is achieved for the first time, to our knowledge, and the coherence and spatial diversity enhanced by photonics are experimentally analyzed and discussed. Furthermore, a comparison with the result of conventional MIMO radar verifies its superior performance in large-scale distribution and high resolution, and extracted features show its great potential in target classification and recognition.

2. PRINCIPLE

A. System Architecture

Figure 1 shows the architecture of the proposed photonics-enabled distributed MIMO radar, including a CO, multiple transmitters (TXs, denoted by TX_m, $m = 1, \ldots, M$, and M is the number of TXs), and multiple RXs (denoted by RX_n, $n = 1, \ldots, N$, and N is the number of RXs), connected via optical fibers in a centralized manner. The CO consists of a clock, photonic orthogonal waveform generator, photonic multi-channel de-chirp processor, analog-to-digital converter, and digital signal processor. The system operates in round-robin transmitting and synchronic receiving modes. Working as the foundation of system coherence, a clock supplies one per pulse second (1PPS) time reference and 10 MHz frequency reference for multi-channel radar signal generation and de-chirped data acquisition. Photonic time-division multiplexing (TDM) waveforms are born from a common reference signal and routed into each fiber link connecting corresponding TXs. Remote TXs/RXs are responsible only for the signal transformation between photonics and electronics, amplification, and radiation or collection. Echoes received by different RXs (RX_n) are loaded onto optical carriers with different wavelengths λ_n, transferred to the CO through different delays τ_{Rn}, and combined for parallel de-chirp processing by the above reference signal. After digitization, the obtained de-chirped echo of each virtual channel, with respect to a pair of TXs and RXs, has a unique time and de-chirp frequency to be distinguished from others for further imaging procedures. In this structure, no additional links for reference signal or control signal transmission are needed, and the share of the reference signal ensures the coherence and simplifies system structure. As a price, some limitations on fiber lengths should be noticed, which are further discussed in the following sections.

A detailed scheme of the proposed radar is depicted in Fig. 2(a). For clarity, the instantaneous frequency–time relationships of different signals, under the circumstance of a 2×2 array, are described in Fig. 2(b). The photonic reference signal is a high duty-cycle linearly frequency-modulated (LFM) pulse with short off-time for the followed switch operation. It is generated by a reconfigurable photonic arbitrary waveform

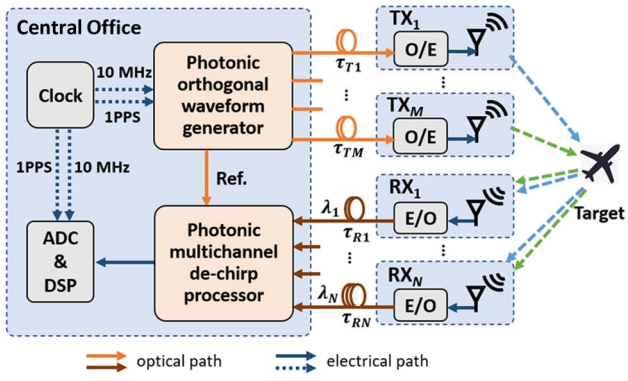

Fig. 1. Architecture of the proposed photonics-enabled distributed MIMO radar. E/O, electro-optical converter; O/E, opto-electrical converter; ADC, analog-to-digital converter; DSP, digital signal processor; Ref., reference signal.

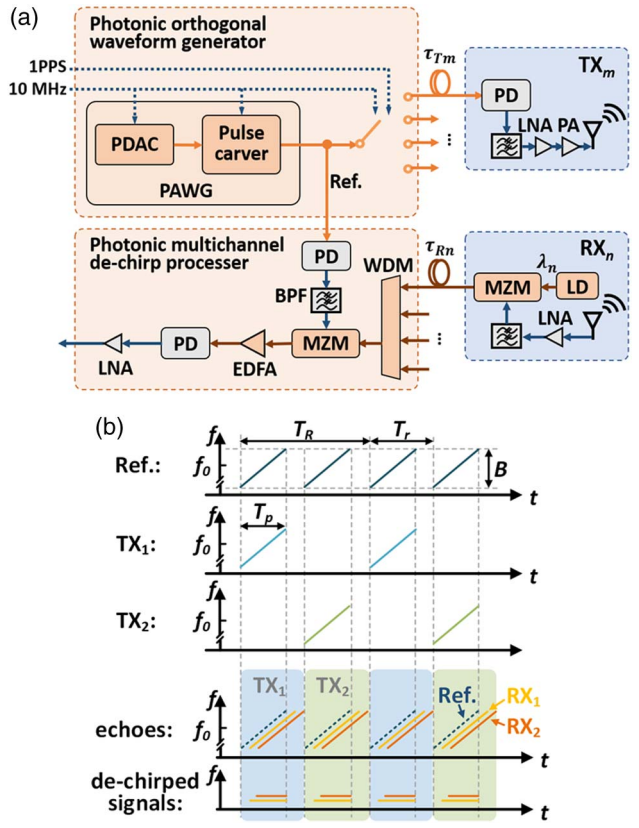

Fig. 2. (a) Schematic diagram of the proposed photonics-enabled distributed MIMO radar. (b) Instantaneous frequency–time diagram of the reference signal, echoes, and de-chirped signals, in the case of a 2 × 2 array. LNA, low-noise amplifier; PA, power amplifier; LD, laser diode; WDM, wavelength-division multiplexer; f_0, B, and T_p, center frequency, bandwidth, and pulse width of the reference signal, respectively; T_r and T_R, pulse repetition periods of the reference signal and emission signal, respectively.

generator (PAWG) including a photonic digital-to-analog converter (PDAC) and a pulse carver for broadband intermediate frequency (IF) signal generation and upconversion, respectively [26]. The LFM waveform during on-time of the reference signal is expressed as

$$\begin{aligned} s_0(t) &\propto \mathrm{rect}\left(\frac{t}{T_p}\right)\cos(2\pi f_0 t + \pi k t^2) \\ &\propto \mathrm{rect}\left(\frac{t}{T_p}\right)\cos[\alpha(t)], \\ \mathrm{rect}\left(\frac{t}{T_p}\right) &= \begin{cases} 1, & |t| \le T_p/2 \\ 0, & |t| \ge T_p/2 \end{cases}. \end{aligned} \tag{1}$$

Here, $\alpha(t) = 2\pi f_0 t + \pi k t^2$, f_0 is the center frequency, k is the chirp rate, and T_p is the pulse width. Then, the photonic reference signal is divided into two parts. One part is converted by a photodetector (PD), filtered by a bandpass filter (BPF), and input to a Mach–Zehnder modulator (MZM) for de-chirp processing. The other part is switched to different fiber links by an electrically controlled optical switch operating at the same pace as the reference signal, thereby allocating per period signal to each TX in turns.

At the TX, the transferred optical signal is converted into an RF signal, which subsequently passes through a BPF and several stages of amplifiers for emission. In this way, in far-field conditions where the distances from different antennas to the same target are similar, echoes received by the RX from all TXs are orthogonal and detachable in time domain if the lengths/delays of the connected fibers are not too different. For simplicity and without loss of generality, the following theoretical analysis is conducted in the case of a single TX.

At RX_n, an antenna collects backscattered echoes from TX_m, written as

$$s_{mn}(t) \propto \mathrm{rect}\left(\frac{t - \tau_{mn} - \tau_{Tm}}{T_p}\right)\cos[\alpha(t - \tau_{mn} - \tau_{Tm})]. \tag{2}$$

Here, τ_{mn} is the travel time from TX_m to RX_n via the target, and τ_{Tm} is the travel time from CO to TX_m. After proper amplification and bandpass filtering, it is fed into an MZM, which is biased at the positive quadrature point, to modulate the optical carrier with a wavelength of λ_n. In this way, the conversion of echoes between electronics and photonics is completed.

The generated photonic echoes from all RXs are then transferred back to the CO through different path delays and combined in a wavelength division multiplexer. The output signal can be given as

$$\begin{aligned} E_m(t) &= \sum_{n=1}^{N} E_{mn}(t) \\ &\propto \sum_{n=1}^{N}\left\{\mathrm{rect}\left(\frac{t - T_{mn}}{T_p}\right)\exp\{j[\omega_n(t - \tau_{Rn})]\}\right. \\ &\quad \left.\times\cos\left\{\frac{\beta_{mn}}{2}\cos[\alpha(t - T_{mn})] + \frac{\pi}{4}\right\}\right\}. \end{aligned} \tag{3}$$

Here, $T_{mn} = \tau_{mn} + \tau_{Tm} + \tau_{Rn}$, τ_{Rn} is the travel time from RX_n to CO, ω_n is the angular frequency corresponding to λ_n, $\beta_{mn} = \pi V_{mn}/V_\pi$ and V_π are, respectively, the modulation index and half-wave voltage of the MZM, and V_{mn} is the amplitude of the echo s_{mn}. Afterwards, it is coupled into another MZM driven by the reference signal, which is also positive quadrature biased, achieving multi-channel photonic de-chirping. The resulting signal is expressed as follows:

$$\begin{aligned} E'_m(t) &\propto \sum_{n=1}^{N}\left\{\mathrm{rect}\left(\frac{t - T_{mn}}{T_p}\right)\exp\{j[\omega_n(t - \tau_{Rn})]\}\right. \\ &\quad \times\cos\left\{\frac{\beta_{mn}}{2}\cos[\alpha(t - T_{mn})] + \frac{\pi}{4}\right\} \\ &\quad \left.\times\cos\left\{\frac{\beta_0}{2}\cos[\alpha(t)] + \frac{\pi}{4}\right\}\right\}, \end{aligned} \tag{4}$$

where $\beta_0 = \pi V_0/V_\pi$ is the modulation index of the MZM, and V_0 is the amplitude of the reference signal s_0. Subsequently, it is sent to a low-speed PD (bandwidth much less than f_0) after being amplified by an erbium-doped fiber amplifier (EDFA), completing parallel de-chirp processing for all echoes. The output de-chirped signal is written as follows:

$$
\begin{aligned}
s'_m(t) &\propto \sum_{n=1}^{N}\left\{\mathrm{rect}\left(\frac{t-T_{mn}}{T_p}\right)\cos^2\left\{\frac{\beta_{mn}}{2}\cos[\alpha(t-T_{mn})]+\frac{\pi}{4}\right\}\right.\\
&\quad\left.\times\cos^2\left\{\frac{\beta_0}{2}\cos[\alpha(t)]+\frac{\pi}{4}\right\}\right\}\\
&\propto \sum_{n=1}^{N}\left\{\mathrm{rect}\left(\frac{t-T_{mn}}{T_p}\right)\{1-\sin\{\beta_{mn}\cos[\alpha(t-T_{mn})]\}\}\right.\\
&\quad\left.\times\{1-\sin\{\beta_0\cos[\alpha(t)]\}\}\right\}\\
&\propto \sum_{n=1}^{N}\left\{\mathrm{rect}\left(\frac{t-T_{mn}}{T_p}\right)\sum_{i=1}^{+\infty}\{J_{2i-1}(\beta_{mn})J_{2i-1}(\beta_0)\right.\\
&\quad\left.\times\cos\{(2i-1)[\alpha(t)-\alpha(t-T_{mn})]\}\}\right\}. \qquad (5)
\end{aligned}
$$

Here, J_i denotes the ith-order Bessel function of the first kind. Substitute $\alpha(t)$ and $\alpha(t-T_{mn})$ into Eq. (5), i.e.,

$$
s'_m(t) \propto \sum_{n=1}^{N}\mathrm{rect}\left(\frac{t-T_{mn}}{T_p}\right)\cos(2\pi kT_{mn}t+2\pi f_0T_{mn}-\pi kT_{mn}^2). \qquad (6)
$$

Here, in the case of small-signal modulation, frequency components above third order are much weaker than that of the first order, which are omitted. The equation suggests that the desired de-chirped signal of each virtual channel is obtained with no requirements for any optical/electrical filtering of high-order sidelobes/harmonics. Furthermore, the frequency, phase, and envelope delay of them are all influenced by fiber delays τ_{Tm} and τ_{Rn}. Consequently, the frequency difference induced by specified fiber lengths is used as the characteristic for channel separation. In other words, the fiber transmissions are used to cache echoes from different channels with different latencies to achieve multi-channel parallel de-chirping. In this way, through the photonic mixer based on cascaded electro-optical (E/O) modulation, the fiber-based optical buffer, and the WDM, echoes of different RXs with the same broadband are converted to de-chirped signals with different and narrow frequency ranges by a common reference signal. Compared with electronic mixers, it has not only a wider bandwidth and better in-band flatness but also stronger capability of multi-channel reception, which leads to a simple system. In the end, the de-chirped signal is amplified and digitized for imaging.

By means of multi-dimensional multiplexing, including time, wavelength, and de-chirp frequency, multi-channel signal generation and echo reception are completed sharing a common reference signal, resulting in a centralized MIMO architecture with high coherence within the fiber network.

Note that during fiber link designing, to avoid spectrum conflict, the de-chirped frequencies of all channels should not be overlapped. Specifically, in the above far-field conditions, for a given interesting scope corresponding to the range of travel time $[\tau_{\mathrm{MIN}},\tau_{\mathrm{MAX}}]$, it should be satisfied that

$$
\tau_{\mathrm{MIN}}+\tau_{TR\_j+1}>\tau_{\mathrm{MAX}}+\tau_{TR\_j},\quad j=1,2,\ldots,MN-1. \qquad (7)
$$

Here, $\tau_{TR\_j}=\tau_{Tm}+\tau_{Rn}$ $(j=1,2,\ldots,MN)$ is the total fiber delay of each virtual channel arranged in ascending order. The channel differences in frequency, phase, and envelope delay, caused by fiber length difference, should be compensated for after channel separation for accurate 3D reconstruction. Another consideration in system design is the type of modulators. For E/O conversion before the fiber transmission in each RX, both direct and external modulations are feasible. Compared with external modulation, direct modulation is energy and cost efficient. But considering that it is usually difficult to provide a large bandwidth and large dynamic range, external modulation is a better choice. For cascaded modulation and multi-channel photonic mixing, external modulation is necessary in the CO. Two mature and widespread commercial external modulators are an MZM and an electroabsorption modulator (EAM). Compared with MZM, EAM has advantages on size, cost, low driving voltage, and photonic integration, and has been widely used in digital communications. However, MZM has relatively better analog performance such as bandwidth, conversion efficiency, linearity, and dynamic range, and is more suitable for radars and other analog systems [27]. Thus, MZM is selected in the proposed system.

B. 3D Imaging Method

The broadband operation of the above system ensures high range resolution. For high angular resolutions in the other two directions, a large 2D aperture is essential. To minimize the number of required transceivers, a super-resolution reconstruction algorithm and the conventional ISAR imaging method are efficiently combined, which are, respectively, based on a sparse array and a synthetic aperture, providing an optimal solution to the trade-off between resolution and complexity [28].

The target is assumed to move at a constant velocity v in synthetic aperture time. The other two directions that are parallel and perpendicular to the motion are defined as azimuth and elevation directions, respectively. Based on the principle of phase center approximation (PCA) [29], $M\times N$ virtual channels form a linear array in elevation. In this geometry, all virtual channels complete high-resolution 2D ISAR imaging simultaneously, depending on the synthetic aperture constituted from target motion. Subsequently, all 2D images are coherently fused for accurate 3D reconstruction, depending on the real aperture constituted by the antenna array perpendicular to the 2D imaging projection plane.

A flowchart of the 3D imaging process is shown in Fig. 3. First, a range profile of the target is reconstructed via fast Fourier transform (FFT) of the digitized signal. Residual video phase (RVP) and range skew are corrected, which are introduced by the de-chirp operation [30], resulting in

$$
\begin{aligned}
S'_m(f) &\propto \sum_{n=1}^{N}V_{mn}\mathrm{sinc}[T_p(f-kT_{mn})]\exp(j2\pi f_0T_{mn})\\
&\propto \sum_{n=1}^{N}\left\{V_{mn}\mathrm{sinc}\left\{T_p\left[f-\frac{2k}{c}(R_{mn}-R_{r\_mn})\right]\right\}\right.\\
&\quad\left.\times\exp\left(j4\pi f_0\frac{R_{mn}-R_{r\_mn}}{c}\right)\right\}. \qquad (8)
\end{aligned}
$$

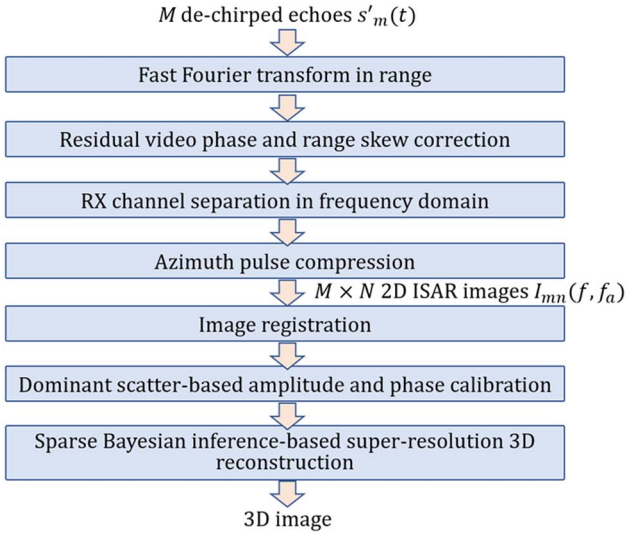

Fig. 3. Flowchart of 3D imaging based on the proposed system.

Here, $R_{mn} = c\tau_{mn}/2$ is the distance from the target to the equivalent antenna phase center (APC), and $R_{r\_mn} = -c \cdot (\tau_{Tm} + \tau_{Rn})/2$ is the reference range determined by the fiber delays of each channel. Thus, the de-chirped echoes of different RXs are separated in frequency domain. Afterwards, the signal is segmented into $M \times N$ channels for azimuth pulse compression. Complex 2D ISAR images are obtained with the pixel values expressed as

$$I_{mn}(f, f_a) \propto V_{mn}\,\mathrm{sinc}\left\{T_p\left[f - \frac{2k}{c}(R_{mn} - R_{r\_mn})\right]\right\} \times \mathrm{sinc}\left[T_a\left(f_a - \frac{2v_{mn}}{\lambda}\right)\right] \times \exp\left(j4\pi f_0 \frac{R_{mn} - R_{r\_mn}}{c}\right), \tag{9}$$

in which f_a is the Doppler frequency, T_a is the overall coherent processing interval, v_{mn} is the radial velocity of the target with respect to APC, and λ is the central wavelength of the radar signal. The first two sinc functions represent the target range and Doppler information. From the equation, the fiber delays induce channel differentiations not only in the scatterer distribution in range ($-2T_p k R_{r\_mn}/c$) but also the additional phase of the pixels ($-4\pi f_0 R_{r\_mn}/c$). Thus, the delay fluctuation during integration time may cause channel decorrelation. Generally, the phase variation is required to be less than 5° for good coherence, and azimuth integration is always completed in a few seconds for ISAR imaging of aerial targets. It could be roughly estimated that the total fiber length within 1 km is satisfied for coherent processing. Different view angles may cause slight differences of power and phase of the same pixel, and part of the latter includes the elevation information used for 3D reconstruction. Before elevation extraction, the above unnecessary differences should be removed through two steps: (1) registration of ISAR images for power distribution uniformization; (2) dominant scatterer-based calibration of the amplitude and phase inconsistency [25]. Specifically, the first step makes scatterers with the same range and Doppler frequency fall into the same pixel, and the second step takes the height of a dominant scatterer as the reference to correct the amplitude and phase inconsistencies between channels. After that, the complex values of the same range-Doppler unit in the ISAR images are rewritten as follows:

$$I_{mn}(f, f_a) \propto V\,\mathrm{sinc}\left[T_p\left(f - \frac{2kR_u}{c}\right)\right]\mathrm{sinc}\left[T_a\left(f_a - \frac{2v_u}{\lambda}\right)\right] \times \exp\left(j4\pi f_0 \cdot \frac{R_{mn}}{c}\right), \tag{10}$$

where R_u and v_u are the uniformed range and radial velocity, respectively. From the equation, the influence of asynchronous receiving due to the differences in fiber lengths of each TX/RX pair, which are the differences in frequency, phase, and envelope delay of the de-chirped signals, is eliminated without knowing the accurate length differences. Finally, 3D reconstruction is completed via elastic net estimation, Bayesian information criterion, and sparse Bayesian inference-based super-resolution imaging.

Note that, although the above theory is under the case of a single scatterer, it is also reliable for a general target, which is usually composed of numerous scatterers and whose echo can be considered as a sum of that of each scatterer. Furthermore, for 3D imaging of more than one target in range direction, two aspects need to be considered: (1) the fiber length design should be based on the imaging scope including all targets (of which the range of the travel time is usually obtained from other radar detection) for reliable multi-channel de-chirping; (2) targets should not overlap in the range-Doppler domain, so that the ISAR imaging of each target is reliable with its range-Doppler information derived from echoes without interference.

The imaging resolutions in three dimensions under the Rayleigh criterion are given as follows:

$$\begin{cases} R_r = 0.886 \cdot \frac{c}{2B}, \\ \theta_a = 0.886 \cdot \frac{\lambda}{2D}, \\ \theta_e = 0.886 \cdot \frac{\lambda}{2L}. \end{cases} \tag{11}$$

Here, no weighting windows are considered. B is the bandwidth of the radar signal; D and L are equivalent apertures in azimuth and elevation directions, referring to the synthetic aperture induced by target motion and the interference baseline formed by the antenna array, respectively.

3. EXPERIMENTS AND RESULTS

To verify the practicability and evaluate the imaging capability of the proposed system, X-band MIMO radar according to the above designs is established, and laboratory and field tests are carried out. The main parameters of the system are reported in Table 1.

In the CO, an oven-controlled crystal oscillator (OCXO) is used as the clock for reference radar signal generation, optical switching, and sampling, which supplies the frequency reference and drives a homemade pulse generator to output synchronized triggers. In the PAWG, an AWG (Tektronix, AWG70002B) outputs 6-bit digital signals into PDAC to generate a photonic IF LFM pulse with a center frequency of

Table 1. Main Design Parameters of the Established System

Parameter	Value
Number of TXs × RXs ($M \times N$)	4 × 4
Center frequency (f_0)	10 GHz
Bandwidth (B)	2 GHz
Pulse width (T_p)	90 μs
Pulse repetition period of the reference signal/emission signal (T_r/T_R)	100 μs/400 μs
Sampling frequency	500 MHz
Sampling resolution	12 bits
Lengths of fiber links connecting TX_m	50 m/50 m/50 m/50 m
Lengths of fiber links connecting RX_n	10 m/110 m/210 m/310 m
Wavelengths of optical carriers of RX_n (λ_n)	1548.52 nm/1549.32 nm/1550.12 nm/1550.92 nm
Horn antenna gain	≈22 dBi

3 GHz and bandwidth of 2 GHz. It is then upconverted by a 13 GHz phase-locked dielectric resonator oscillator (PLDRO) to drive the pulse carver. The resulting signal is evenly divided into two branches. One branch is input to a PD for opto-electric conversion, obtaining the reference signal. The other one is allocated to four TXs passing by a 1 × 4 electrically controlled optical switch (EO space) and corresponding fiber links. The remote TXs (four TXs and four RXs) are established according to the architecture in Fig. 2(a). Each TX converts the transmitted signal to an RF signal and further amplifies it to about 11 W for emission. The backscattered echoes from TXs are collected by all RXs simultaneously. At each RX, they are E/O converted, amplified, and finally transferred back to the CO. After combination, echoes on the wavelength-division carriers are modulated by the same reference signal in a shared MZM, achieving photonic de-chirping together. Last, the output signal is converted after proper amplification, filtered for anti-aliasing and digitized for processing.

Before field tests, measurements of some influences on 3D imaging from the radar, such as inter-pulse and inter-channel coherences, inter-channel interference, and range resolution, are conducted in a microwave anechoic chamber. Here, the first one directly affects the equivalent apertures' effectiveness in azimuth and elevation directions, and further relevant resolutions.

First, a back-to-back test is carried out to evaluate the inter-pulse and inter-channel coherences and the inter-channel interference. A static trihedral corner reflector (TCR) is employed as an ideal point scatterer. Because the target ranges in the chamber and outfield are different, a 1 km length fiber delay line is inserted before the PD, which acts on the photonic reference signal to adjust equivalent ranges, so that the frequencies of the de-chirped signals of four RXs fall into the passband of the anti-aliasing filter. Since the fiber delay fluctuations arising therefrom are the same for all channels, it will not affect the channel coherence. In addition, four groups of attenuators with roughly the same values are added after the receiving antennas to reduce the powers of received echoes within the dynamic range of the receiving links. Afterwards, de-chirped signals of all 16 virtual channels are recorded. The spectrum of one period signal that falls into the anti-aliasing filter's passband and corresponds to one TX and four RXs is shown in Fig. 4(a). The results imply that each RX occupies an exclusive segment of spectrum with no obvious intermodulation among them. The small signal next to RX_1 is from sundries in the chamber, which is in sight of only the RX_1 antenna. To analyze the coherence between pulses within 20 s (a sufficient time for azimuth coherent integration in outfield imaging), the phase of the peak point of each RX in each cycle is extracted, and the result of RX_1 is shown in Fig. 4(b) (blue line). Despite the additional fiber delay, an acceptable phase variation below 2° is obtained. The phase differences between channels are calculated for coherence assessment, and the worst result appearing between RX_1 and RX_4 is also shown in Fig. 4(b) (red line). Due to the short integration time required, the drifts of the phase differences are no more than 1°, which is absolutely satisfied for performing 3D reconstruction. As a converse interpretation, considering the same tolerable drift below 5° in azimuth and elevation directions, both lengths and their maximum differences of connecting fibers could be extended to above 1 km, thereby supporting a large-scale antenna array and better resolution in elevation.

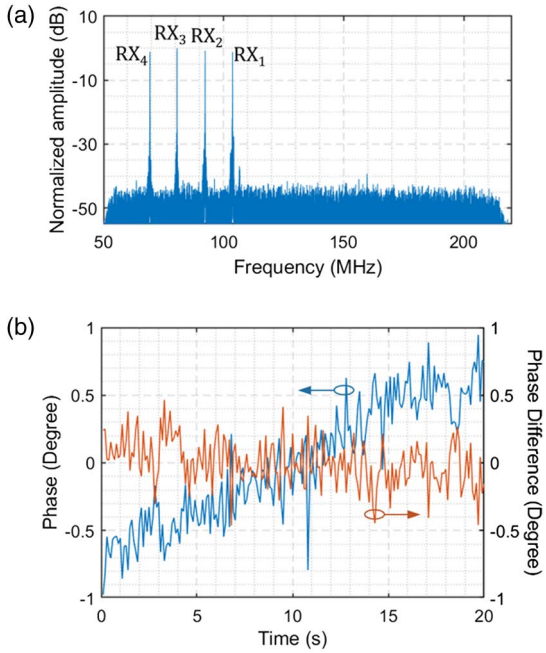

Fig. 4. Test results of a static TCR. (a) Spectrum of one period de-chirped signal relative to one TX and four RXs. (b) Phase drift of RX_1 (blue line) and phase difference drift between RX_1 and RX_4 (red line).

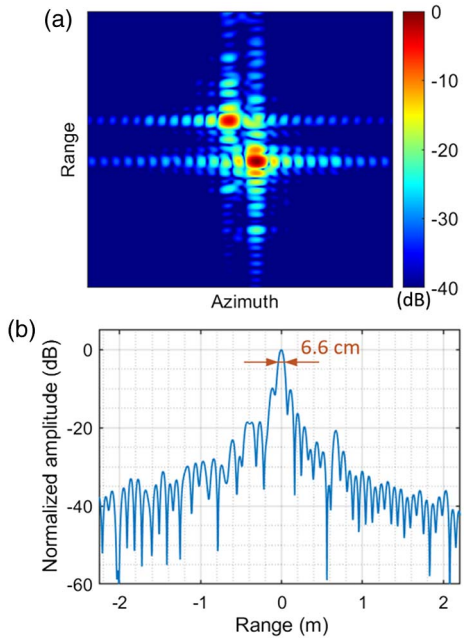

Fig. 5. Test results of a pair of rotating TCRs. (a) Single-channel ISAR image. (b) Range slice of one TCR.

Second, multi-channel ISAR imaging of a pair of rotating TCRs is completed for range resolution measurement and inter-channel interference survey. There are 16 2D images obtained, and no clutter is observed, one of which is sketched in Fig. 5(a). The range slice of one TCR is depicted in Fig. 5(b). A 3 dB width of 6.6 cm is achieved, consistent with the theoretical value.

Afterwards, a field test is carried out through 3D imaging of a non-cooperative airplane, Boeing 777, during landing. The established MIMO radar is installed on a bridge near an airport, where a flight path passes [Fig. 6(a)]. A photograph and layout of the radar are, respectively, presented in Figs. 6(b) and 6(c), including a CO, four TXs, and four RXs. Sixteen APCs form a uniform linear array (ULA) with the same spacing of d, which is set to 0.6 m in the experiment; thus, the longest baseline is 9 m. The radiation directions of all antennas are substantially parallel, and are perpendicular to the flight path with a similar elevation angle of about 35°. Because the ULA could not be aligned perpendicular to the flight path, the azimuth is about 20° between the ULA and the radiation direction. The resulting maximum of the effective baseline in elevation is 4.85 m, corresponding to the Rayleigh resolution of 0.16°.

First, the backscattered echoes from all TXs are received by all RXs and recorded after photonic de-chirping. Through integration of 1000 durations, namely, 0.4 s, in each virtual channel, 16 2D ISAR images are obtained, one of which is shown in Fig. 7 accompanied with a photograph of the imaged airplane. According to an estimated velocity of the airplane of 63.5 m/s [28], the resulting azimuth resolution is approximately 0.03°. From the frequency of the de-chirped signal (around 139.54 MHz in TX_1/RX_1 channel) and corresponding fiber lengths (50 m/10 m), the distance from the radar to the airplane can be derived as about 896.9 m. Compared with

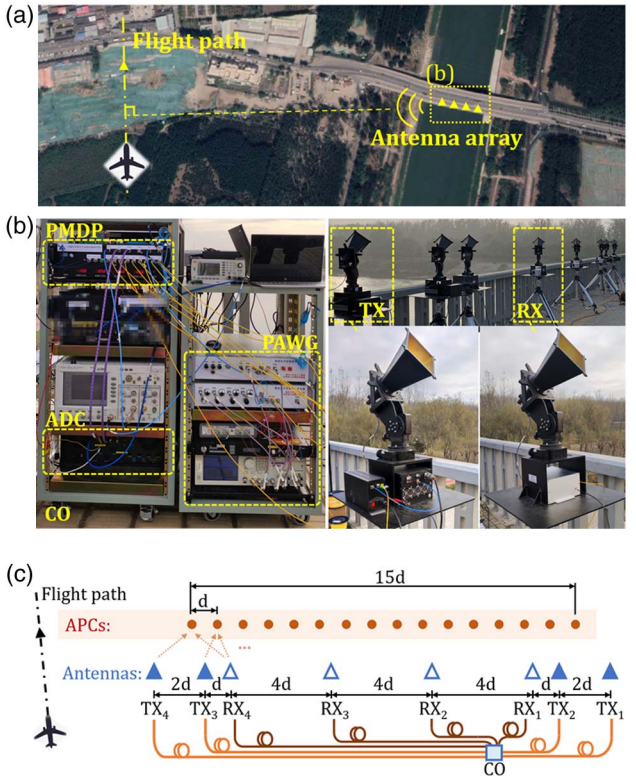

Fig. 6. (a) Overhead topology of distributed MIMO radar on a bridge and the flight path passing by. (b) Photograph of distributed MIMO radar, including a CO, four TXs, and four RXs. (c) Layout of distributed MIMO radar and corresponding APCs.

the photograph, two engines on both sides of the fuselage are clearly visible, whereas two stabilizers in the empennage are too dim to been recognized as the vertical or horizontal one.

Second, 3D reconstructions employing ISAR images from different channels are completed to evaluate the imaging capability and analyze the influence of some system configurations on it, such as sensor quantity, baseline length, and antenna spacing. The obtained 3D images from two TXs–four RXs (i.e., TX_1, TX_2, and RX_1 to RX_4) and four TXs–four RXs

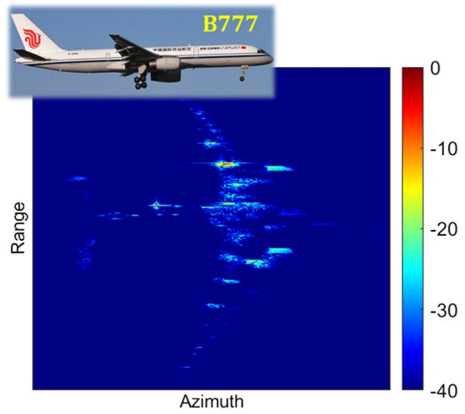

Fig. 7. Photograph and single-channel ISAR image of the imaged airplane.

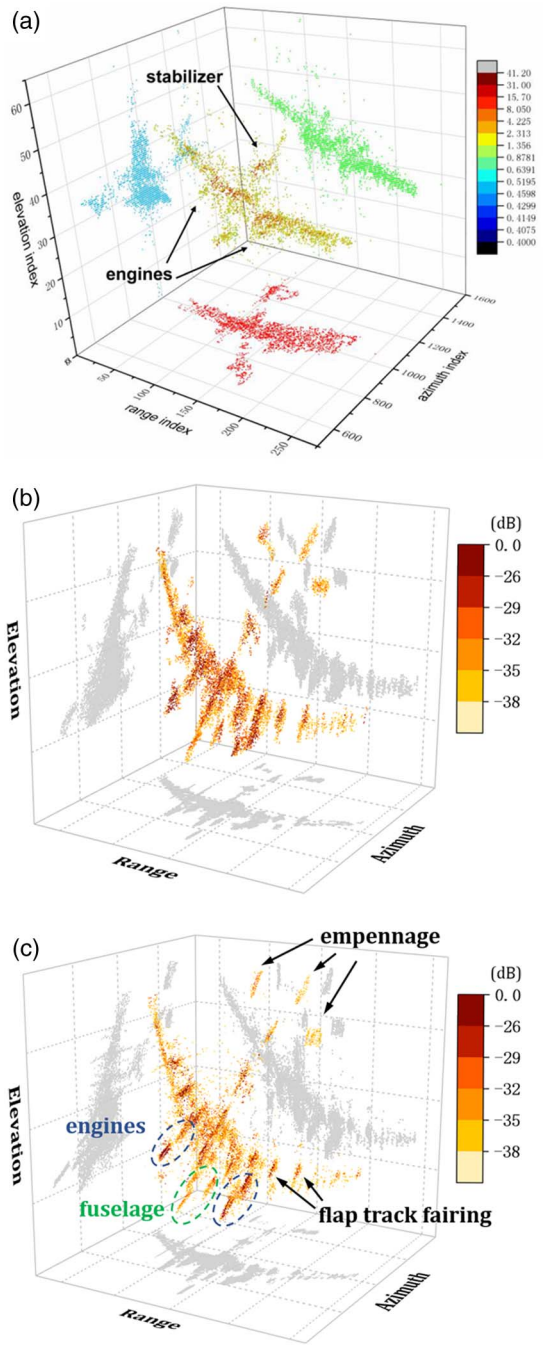

Fig. 8. Comparison of reconstructed 3D images obtained by conventional MIMO radar and established MIMO radar: (a) the former including two TXs and four RXs with a maximum baseline of 1.3 m [28]; (b) the latter including two TXs and four RXs with a maximum baseline of 4.2 m; (c) the latter including four TXs and four RXs with a maximum baseline of 9 m.

(i.e., TX_1 to TX_4 and RX_1 to RX_4) are shown in Figs. 8(b) and 8(c), respectively, with corresponding maximum baselines of 4.2 m and 9 m. As a comparison, a 3D image acquired before by conventional MIMO radar in a similar operation environment (i.e., same test site and same flight path) is also presented in Fig. 8(a) [28]. Three projections of all 3D images are presented. The radar includes two TXs and four RXs with a bandwidth of 500 MHz and maximum baseline of 1.3 m. In these images, the postures of the airplanes are all displayed due to a good focus in elevation. However, it can be seen from the comparison of Figs. 8(b) and 8(a), with the same quantity of antennas, both range and elevation resolutions are significantly improved in the proposed radar, due to the wider bandwidth and longer baseline brought by photonics. Despite the super-resolution imaging algorithm, constantly increasing the array spacing for a longer baseline is inadvisable, and would ultimately lead to elevation ambiguity. An alternative is increasing the sensor quantity. A comparison of the results from a further lengthened baseline in this way can be seen in Figs. 8(b) and 8(c). A sharper image is obtained and more features are observed in Fig. 8(c), such as flap track fairings under the wings and two horizontal and one vertical stabilizer in the empennage, which are not seen in the 3D image from conventional radar [Fig. 8(a)] or the 2D ISAR image from the proposed radar (Fig. 7). In addition, the fuselage and engines all appear to consist of several linear scatterers at different heights, identical to the cases of typical cylindrical structures under lateral illumination. To quantitatively compare the image sharpness, Rényi entropies of the 3D images in Figs. 8(b) and 8(c) are calculated as 1.19 and 0.92, respectively [31,32]. The results further demonstrate the improvement in image quality. It should be noted that, even though the sharpness of the image is improved, it still looks less fine than visual images. It is mainly owed to two aspects: (1) the microwave imaging method employs active coherent detection, such as synthetic aperture and array aperture, which brings unavoidable speckle noise [33]; (2) the inherent electromagnetic scattering features of the airplane lead to echo energy mainly from some specific structures where specular reflection or edge diffraction takes place. Thus, the 3D image is composed of just sparsely distributed strong scatterers. However, due to its superiority of long-distance sensing and all-time and all-weather effectiveness over optical imaging, the microwave imaging of radar arrays is an essential approach in applications such as area surveillance, surveying and mapping, and target classification and identification.

For 3D imaging of a more distant target, under the assumption of the same airplane appearing in the same angle of view with the same velocity, the azimuth and elevation angular resolutions would not change as long as the integration time and the layout of the antenna array are unvaried and the attendant power issues are solvable. However, the sharpness of the image in these two directions would decrease due to deterioration of distance-dependent spatial resolutions. To improve the azimuth resolution, increasing integration time is an effective approach that would enlarge the synthetic aperture while increasing the difficulty of motion compensation. The maximum size of the synthetic aperture is limited by the 3 dB beamwidth of the antenna, which is 12° in the system. It means the distance could increase up to 400 times without deteriorating the spatial resolution in azimuth direction. To improve the elevation resolution, increasing the antenna spacing to obtain a longer baseline is an effective approach. Considering the limitations in the previous analysis on the fiber lengths and their maximum difference, the maximum acceptable

distance between TX_1 and TX_4 is 2 km with an APC spacing of 111 m. As a result, the distance could increase up to 185 times without deteriorating the spatial resolution in elevation direction.

In summary, all these results illustrate that, enabled by photonics, more TXs and longer baselines support better angular resolution and more sophisticated features, which are exactly indispensable for target monitoring and identification.

4. CONCLUSION

To achieve high-resolution 3D imaging and overcome the trade-off between low system complexity and large 2D apertures, photonics-enabled distributed MIMO radar is experimentally demonstrated. Taking advantage of microwave photonics for broadband operation, multi-dimensional multiplexing, and highly coherent fusion, together with array ISAR-based super-resolution 3D reconstruction methods, a simple and efficient system is implemented, and high resolutions in all three dimensions are achieved. Both laboratory measurements and field tests are conducted. 3D images of a non-cooperative airplane are obtained, and a comparison with the result from electronic radar is also carried out. Owing to remarkable resolution improvement, more geometric features of the target are extracted along with lengthening baselines and increasing TXs. The outstanding performance validates the practicability of photonics-enabled MIMO radar and its imaging capability surpassing conventional systems, which may provide a new way for future radar networks in distributed detection and target recognition and monitoring.

Funding. National Natural Science Foundation of China (61690191, 62101536).

Disclosures. The authors declare no conflicts of interest.

Data Availability. Data underlying the results presented in this paper are not publicly available at this time but may be obtained from the authors upon reasonable request.

REFERENCES

1. G. Wang, X. Xia, and V. C. Chen, "Three-dimensional ISAR imaging of maneuvering targets using three receivers," IEEE Trans. Image Process. **10**, 436–447 (2001).
2. G. Duan, D. Wang, X. Ma, and Y. Su, "Three-dimensional imaging via wideband MIMO radar system," IEEE Geosci. Remote Sens. Lett. **7**, 445–449 (2010).
3. C. Ma, T. S. Yeo, H. S. Tan, J. Li, and Y. Shang, "Three-dimensional imaging using collocated MIMO radar and ISAR technique," IEEE Trans. Geosci. Remote Sens. **50**, 3189–3201 (2012).
4. Y. Wang and X. Chen, "3-D interferometric inverse synthetic aperture radar imaging of ship target with complex motion," IEEE Trans. Geosci. Remote Sens. **56**, 3693–3708 (2018).
5. Z. Zhu, L. Kuang, and F. Xu, "Microwave imaging of non-rigid moving target using 2D sparse MIMO array," IEEE Access **7**, 146240 (2019).
6. L. Kang, Y. Luo, Q. Zhang, W. Liu, and B. Liang, "3-D scattering image sparse reconstruction via radar network," IEEE Trans. Geosci. Remote Sens. **60**, 5100414 (2022).
7. G. Serafino, F. Scotti, L. Lembo, B. Hussain, C. Porzi, A. Malacarne, S. Maresca, D. Onori, P. Ghelfi, and A. Bogoni, "Toward a new generation of radar systems based on microwave photonic technologies," J. Lightwave Technol. **37**, 643–650 (2019).
8. M. Akcakaya and A. Nehorai, "MIMO radar detection under phase synchronization errors," in *Proceedings IEEE International Conference on Acoustics, Speech, and Signal Processing* (2010), pp. 2578–2581.
9. J. D. McKinney, "Technology: photonics illuminates the future of radar," Nature **507**, 310–312 (2014).
10. P. Ghelfi, F. Laghezza, F. Scotti, G. Serafino, A. Capria, S. Pinna, D. Onori, C. Porzi, M. Scaffardi, A. Malacarne, V. Vercesi, E. Lazzeri, F. Berizzi, and A. Bogoni, "A fully photonics-based coherent radar system," Nature **507**, 341–345 (2014).
11. F. Zhang, Q. Guo, and S. Pan, "Photonics-based real-time ultra-high-range-resolution radar with broadband signal generation and processing," Sci. Rep. **7**, 13848 (2017).
12. A. Wang, J. Wo, X. Luo, Y. Wang, W. Cong, P. Du, J. Zhang, B. Zhao, J. Zhang, Y. Zhu, J. Lan, and L. Yu, "Ka-band microwave photonic ultra-wideband imaging radar for capturing quantitative target information," Opt. Express **26**, 20708–20717 (2018).
13. R. Li, W. Li, M. Ding, Z. Wen, Y. Li, L. Zhou, S. Yu, T. Xing, B. Gao, Y. Luan, Y. Zhu, P. Guo, Y. Tian, and X. Liang, "Demonstration of a microwave photonic synthetic aperture radar based on photonic-assisted signal generation and stretch processing," Opt. Express **25**, 14334–14340 (2017).
14. D. Wu, S. Li, X. Xue, X. Xiao, S. Peng, and X. Zheng, "Photonics based microwave dynamic 3D reconstruction of moving targets," Opt. Express **26**, 27659–27667 (2018).
15. A. Malacarne, S. Maresca, F. Scotti, P. Ghelfi, G. Serafino, and A. Bogoni, "Coherent dual-band radar-over-fiber network with VCSEL-based signal distribution," J. Lightwave Technol. **38**, 6257–6264 (2020).
16. S. Maresca, A. Malacarne, P. Ghelfi, and A. Bogoni, "Information diversity in coherent MIMO radars," in *IEEE Radar Conference* (2021), pp. 1–6.
17. S. S. S. Panda, T. Panigrahi, S. R. Parne, S. L. Sabat, and L. R. Cenkeramaddi, "Recent advances and future directions of microwave photonic radars: a review," IEEE Sens. J. **21**, 21144–21158 (2021).
18. X. Ye, F. Zhang, Y. Yang, D. Zhu, and S. Pan, "Photonics-based high-resolution 3D inverse synthetic aperture radar imaging," IEEE Access **7**, 79503–79509 (2019).
19. B. Gao, F. Zhang, G. Sun, Y. Xiang, and S. Pan, "Microwave photonic MIMO radar for high-resolution imaging," J. Lightwave Technol. **39**, 7726–7733 (2021).
20. S. Maresca, F. Scotti, G. Serafino, L. Lembo, A. Malacarne, F. Falconi, P. Ghelfi, and A. Bogoni, "Coherent MIMO radar network enabled by photonics with unprecedented resolution," Opt. Lett. **45**, 3953–3956 (2020).
21. G. Serafino, S. Maresca, L. Mauro, A. Tardo, A. Cuillo, F. Scotti, P. Ghelfi, P. Pagano, and A. Bogoni, "A photonics-assisted multi-band MIMO radar network for the port of the future," IEEE J. Sel. Top. Quantum Electron. **27**, 6000413 (2021).
22. X. Xiao, S. Li, X. Xue, L. Xing, S. Peng, X. Zheng, and B. Zhou, "Photonics-assisted broadband distributed coherent aperture radar for high-precision imaging of dim-small targets," IEEE Photon. J. **11**, 5502709 (2019).
23. H. Wang, S. Li, X. Xue, X. Xiao, and X. Zheng, "Distributed coherent microwave photonic radar with a high-precision fiber-optic time and frequency network," Opt. Express **28**, 31241–31252 (2020).
24. F. Berland, T. Fromenteze, D. Boudescoque, P. Di Bin, H. H. Elwan, C. Aupetit-Berthelemot, and C. Decroze, "Microwave photonic MIMO radar for short-range 3D imaging," IEEE Access **8**, 107326 (2020).
25. J. Dong, F. Zhang, Z. Jiao, Q. Sun, and W. Li, "Microwave photonic radar with a fiber-distributed antenna array for three-dimensional imaging," Opt. Express **28**, 19113–19125 (2020).
26. J. Liao, B. Chen, S. Li, X. Yang, X. Zheng, H. Zhang, and B. Zhou, "Novel photonic radio-frequency arbitrary waveform generation based on photonic digital-to-analog conversion with pulse carving," in *Conference on Lasers and Electro-Optics* (2015), paper STh4F.4.

27. V. J. Urick, J. D. McKinney, and K. J. Williams, *Fundamentals of Microwave Photonics* (Wiley, 2015).
28. Z. Jiao, C. Ding, L. Chen, and F. Zhang, "Three-dimensional imaging method for array ISAR based on sparse Bayesian inference," Sensors **18**, 3563 (2018).
29. A. Bellettini and M. A. Pinto, "Theoretical accuracy of synthetic aperture sonar micronavigation using a displaced phase-center antenna," IEEE J. Oceanic Eng. **27**, 780–789 (2002).
30. M. A. Richards, *Fundamentals of Radar Signal Processing*, 2nd ed. (2005).
31. T. J. Kragh, "Minimum-entropy autofocus for three-dimensional SAR imaging," Proc. SPIE **7337**, 73370B (2009).
32. J. R. Fienup, "Synthetic-aperture radar autofocus by maximizing sharpness," Opt. Lett. **25**, 221–223 (2000).
33. Y. Sun, W. Jiang, J. Yao, and W. Li, "SAR target recognition using cGAN-based SAR-to-optical image translation," Remote Sens. **14**, 1793 (2022).